Article

Assessment of Pore Connectivity and Representative Elementary Volume Size in Marine-Continental Transitional Shale

Jinfeng Xie, Yong Li,* Derek Elsworth, and Zhejun Pan

Read Online

ACCESS | Metrics & More | Article Recommendations

ABSTRACT: Directly obtaining representative pore structure information is important to understand subsurface shale gas storage and production, while acquiring large-scale and high-resolution images using a single imaging tool is plausible as there is always a trade-off between the resolution and field-of-view. We report a new method to define representative elementary volumes (REV) of a shale pore system and define pore structural parameters of diameter, surface area, porosity, and other features. Automated ultrahigh resolution scanning electron microscopy, integrated with a modular automated processing system (MAPS), was used to image pore distribution in two dimensions. Focused ion beam (FIB) milling was further utilized to construct a true three-dimensional digital image, on which the REV analysis was then carried out. The results show that (i) pores are mainly developed in organic matter (OM) and as interparticle inorganic pores and (ii) the diameter of inorganic pores is slightly larger than those in OM. The pore network coordination number, representing the average number of pores that are connected to a specific pore, indicates that the pores can be either clustered within mainly OM pores or more widely connected by slit-like pores and throats in minerals. Extracting cubic sub-blocks, ranging from 500 to 5000 nm in edge dimension, defines the minimum REV as ∼4000 nm, as measured using minimum and maximum pore sizes, surface areas, and shape factors. Combined FIB and MAPS provide insight into pore morphology and connectivity at multiple scales with the reconstructed digital rock used to determine representative REV sizes. Such results are useful in understanding the pore structure in shales and for the rapid acquisition of pore structure distributions.
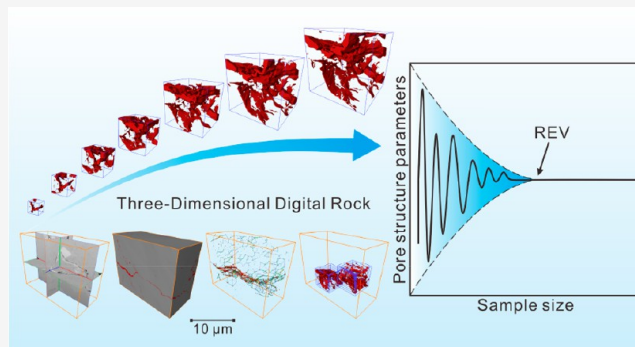
1. INTRODUCTION

The nature of shale pore networks, including pore morphology, connectivity, and distribution (both in organic matter and mineral hosts), is a key factor affecting subsurface transport and storage in shales for the recovery of CH_4 as a transitional fuel,[1−7] storage of H_2,[8,9] sequestration of CO_2, and geo-mechanical behaviors like tunnel excavation and slope engineering.[10−13] Different experimental techniques have been used to characterize the pore structure of shales.[14] The currently available imaging tools for high-resolution three-dimensional (3D) analysis of rock samples include non-destructive instruments, such as X-ray computed tomography (CT), and destructive instruments such as dual beam Focused Ion Beam and Scanning Electron Microscope (FIB-SEM) tomography.[15,16] However, the higher resolution provided by advanced imaging techniques such as FIB-SEM and nano-CT inevitably limits the study field-of-view (FOV). Meanwhile, instruments with larger FOV, such as micro-CT, provide much lower resolution, so they cannot resolve most of the pores in shale. Therefore, it is critical to determine the optimal sample size and resolution for obtaining the structural characteristics of shale pores. To ensure that analysis of the micronano pore

systems is sufficiently representative, and in order to simplify the quantification of transport and storage characteristics, it is necessary to select a reasonable unified representative elementary volume (REV) (the smallest size that can represent the key characteristics of a macroscale sample) for the pore systems.[17−21] Key physical properties of porosity and permeability are common proxy targets that are used to evaluate the appropriate REV while neglecting the intrinsic details of the pore structure.[17−19,22−25] Therefore, in the study of pore structure characterization, it should focus on each pore itself and considering each pore's own characteristics in the assessment of REV. Compared to marine shales, marine-continental transitional shales contain high clay mineral contents with relatively complex mineral compositions, and
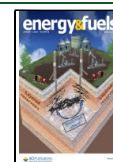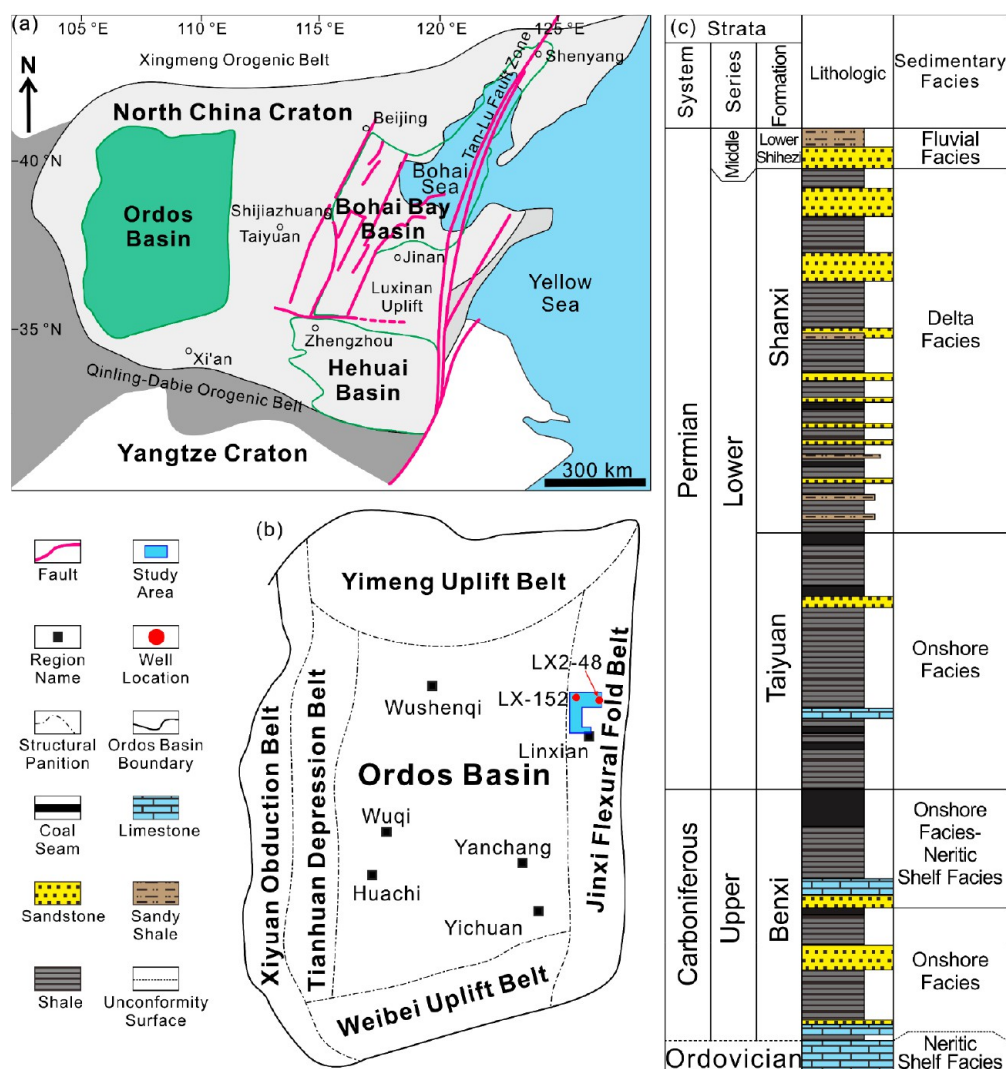
Figure 1. Sampling location and its geological setting. (a) Location of the Ordos Basin in the North China Craton (modified with permission from ref 36. Copyright 2018 Springer Nature); (b) tectonic divisions of the Ordos Basin (modified from ref 33. Copyright 2023 American Chemical Society); (c) lithologic section and depositional environment in the Linxing area.

fully and correctly understanding the pore connectivity is important in predicting the potential commercial production of gas from such shales.[26−31]

In this study, both two-dimensional (2D) and three-dimensional (3D) pore morphology, size, and connectivity in two transitional shale samples from the eastern Ordos Basin, China, have been studied; we use high-resolution SEM imaging combined with FIB milling, with postprocessing by a modular automated processing system (MAPS). Based on pore structure parameters recovered in the microscale range, the minimum REV size of the shale pore system is defined. The detailed segmentation of pores and rock matrix based on grayscale information was conducted after denoising and binarizing the various image data sets recovered from the analytical methods. Then the smallest REV that can reasonably represent the pore system is defined by taking the maximum and median values of various pore structure parameters as an indicator.

2. MATERIALS AND METHODS

2.1. Samples. Two transitional shale samples were recovered from the Linxing area on the eastern margin of the Ordos Basin (Figure 1). The study area is projected to host good transitional shale gas resources, while its production is yet to be confirmed due to its complex mineral composition and doubtful physical properties.[32] The samples were collected from wells LX2−48 (sample V1) and LX-152 (sample V2), part of the Carboniferous-Permian Taiyuan Formation. The Taiyuan Formation is mainly barrier islands, tidal flats, and lagoon sedimentary environments.[33] This formation is composed of a set of interbedded sediments including coal seams, shales, and tight sandstones.[34,35] The burial depths of the collected samples are1998.18 and 1761.30 m, and the shale in the study area is transitioning within the mature to postmature hydrocarbon generation stage.[32] Total organic carbon (TOC) content was measured on a CS230 Carbon/Sulfur instrument from LECO Corporation with a precision of 0.5%. The TOC contents of the two samples are 2.47% and 1.51%, respectively.

2.2. Quantitative Evaluation of Minerals (QEMSCAN). Automated mineralogical analysis by QEMSCAN was used to nondestructively quantify the amount, type, and distribution of minerals. Samples were run on an FEI Qemscan 650F instrument at a resolution of 10 nm at the China National Offshore Oil Corporation

(CNOOC) in Tianjin. The equipment uses backscattered electron imaging and energy-dispersive X-ray analysis (EDX) to obtain the mineralogical composition of different phases.[37−39]

2.3. MAPS. To ensure that the samples are representative, we selected SEM images that contain both organic matter and clay minerals. A dual-beam Helios NanoLab 650 instrument (FEI company) was employed, and automated SEM image acquisition and image-stitching are used to create a composite image representing a large area at high-resolution (of SEM images).[40−42] More than 5000 high-resolution SEM images (10 nm/pixel) were combined into a large FOV image, allowing the pore morphology and distribution at different scales (>10 nm) to be observed.[43] Samples with a thickness of 2−5 mm were prepared by ion polishing followed by the deposition of a carbon conductive film (10−20 nm thick) coating. All the images were stitched together to get a broad view of the samples; the frames for the two samples are 15.65 × 14.42 and 0.8152 × 0.7346 mm for samples V1 and V2, representing ultralow porosity/organic matter (OM)-host and relatively high porosity/mineral matter (MM)-host samples, respectively.

2.4. FIB-SEM. The two samples were also analyzed by the FEI Helios NanoLab 650 Dual-Beam FIB-SEM instrument, allowing 3D imaging. The sample is milled to successive depths of 10 nm by an ion beam, with each image having a detected area of 10 × 10 nm, with the total volume for the two samples being 10 μm × 10 μm × 5 μm (V1) and 18 μm × 8.5 μm × 14 μm (V2). In this process, the serial sectioning was performed using a 30 kV gallium ion beam with a beam current of 790 pA and slice spacing of 20 nm. The SEM instrument generates images of the newly milled shale surface in situ with a resolution of 10 nm at 3 kV accelerating voltage and a working distance of 4 mm.[44−46]

2.4.1. Image Processing. To ensure the representativeness of the reconstructed area and to eliminate the impact of the background edges, the largest inscribed cuboid in the central area of the original 3D data from FIB-SEM was extracted. The nanotomographic images were imported into AVIZO software for image processing. First, the obtained images were registered, aligned, and cropped. Then the Non-Local Means Filter algorithm was used to filter and optimize the image data sets and remove image noise to improve the signal-to-noise ratio (SNR).[47,48] Image segmentation was performed using interactive threshold segmentation based on the grayscale information on the image.[31] Phases such as the pores, OM, and MM were individually segmented and quantified.

After pore extraction, the Pore Network Model (PNM) application module in the AVIZO software is used to reconstruct the 3D pore network model based on the maximal-balls algorithm.[6] In the model, spheres represent the pores, and cylinders represent the throats connecting the pores. The size of the sphere is related to the equivalent diameter of the pore, and the diameter of the cylinder is related to the equivalent diameter of the throat. Using the Label Analysis module to calculate the obtained pore three-dimensional data, the shape and physical parameters of each pore and pore throat can be obtained, including equivalent diameter, volume, and coordination number related to connectivity.[49]

2.4.2. Three-Dimensional Pore Shape Factor. In 3D space, the shape factor can reflect the regularity of the outer contour of the object (the shape factor of a perfect sphere is 1).[50] The higher the difference between the shape factor and 1, the rougher the pore boundary. In AVIZO software,[51] the shape factor can be calculated as

$$\text{Shape Factor} = \frac{S^3}{36 \times \pi \times V^2} \tag{1}$$

where S = pore surface area, nm^2; V = pore volume, nm^3.

2.4.3. REV Acquisition. The concept of an REV was originally proposed by Bear in 1972 (Figure 2) as the smallest size/sample that can represent the macroscale response.[52−57] Figure 2 is a schematic of an REV. The erratic fluctuations in the property of interest (e.g., porosity and permeability) reduce with the increasing sample size (region I). The fluctuations in region II are relatively insensitive to small changes in the sampled volume, suggesting that some properties
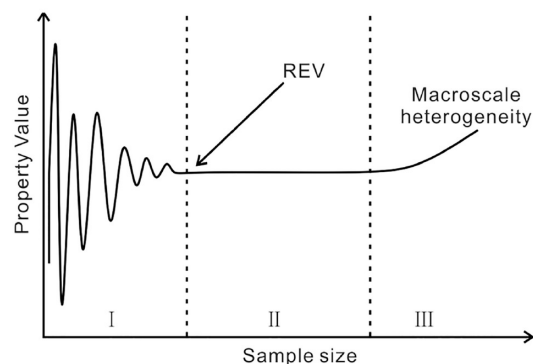

Figure 2. Graphical representation of the concept of representative elementary volumes (REV) for a specific property (modified with permission from ref 57. Copyright 2019 Elsevier).

of the sample become invariant with sample size. Therefore, the left boundary of region II represents the minimum REV. With a further increase in sample size beyond region II, some properties of some porous media may again change (region III).

As an alternative to using unified parameters, such as porosity and permeability, to define the minimum REV, this study uses pore structure parameters at the micro scale to find the REV of the pore system. Sub-blocks with different volumes and sizes were extracted from the whole rock, with their pore and matrix structures reconstructed and displayed in 3D. A total of 11 pore structure parameters of different sub-blocks were statistically analyzed, including median pore volume, minimum pore volume, maximum pore volume, median pore diameter, minimum pore diameter, and maximum pore diameter, porosity, average pore shape factor, minimum pore surface area, maximum pore surface area, and median pore surface area.

3. RESULTS

Here we report the mineral composition and distributions acquired by QEMSCAN to understand the strong mineralogical heterogeneity of shales. We examine pore types and connectivity at a continuous scale using MAPS with 3D digital rock reconstruction from the FIB data to present the results of the pore size distribution and morphology.

3.1. Mineral Compositions. The QEMSCAN results show that the mineralogical distribution is highly heterogeneous at the um scale for the two samples (Figure 3) and that the minerals are distributed randomly. The shales comprise mainly quartz (37.5% ~ 49.1%), kaolinite (11.9% ~ 18.8%), muscovite (5.5% ~ 14.1%), and albite (3.8% ~ 6.2%). The presence of Illite and muscovite is relatively limited, mostly distributed in agglomerates (Figure 3a), while a few are scattered around large-particle minerals (Figure 3d). A small number of scattered K-feldspars are present in clumps with smaller grains, as can be seen in Figure 3a,b, representing the low-porosity sample. In the high-porosity sample, Figure 3c, the crystal grains of quartz and clay minerals are larger and contain scattered kaolinite and albite. The mineral crystal grains in Figure 3d are smaller, with clay minerals packed among the quartz grains. For high-density minerals, siderite is the only one developed in the two samples, and the pyrite content is low.

3.2. Pore Type and Pore Structure. This study uses the classification scheme for the Barnett shale by Loucks[58,59] to divide matrix pores into three types: OM pores, interparticle pores (interP pores), and intraparticle pores (intraP pores), according to their genetic origin. This section uses data
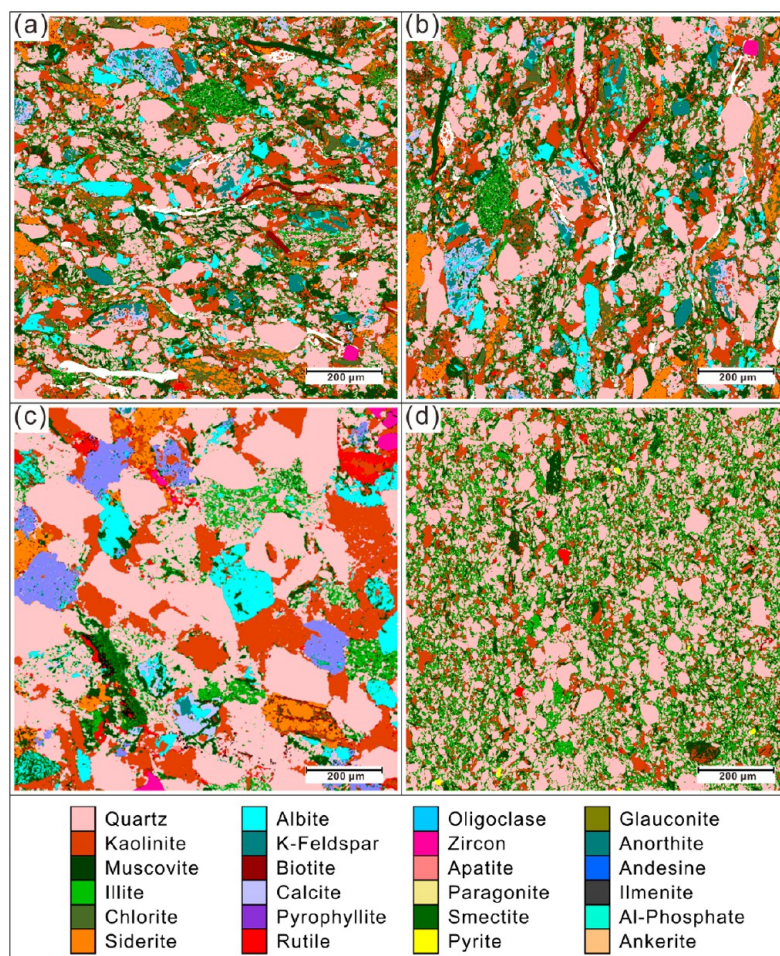
Figure 3. Mineral distribution of the samples acquired by QEMSCAN. (a, b) from sample V1 representing low porosity; (c, d) from sample V2 representing high porosity.

provided by the MAPS technique, which is capable of observing pores above 10 nm. A large number of nano- to micrometer sized pores are developed in the OM and mineral matrix. In the low-porosity sample V1, OM pores are mainly developed, while inorganic pores are less abundant. The OM is in the form of long thin strips and scattered clumps (Figure 4). The OM pores exist in the OM strips (Figure 4e). Some interparticle pores are clustered between clay minerals (Figure 4e,h). Pyrite can be seen aggregated and distributed inside the strips of OM (Figure 4a,b). Some of the siderite develops in the area where the clay minerals are in contact with the OM strips (Figure 4b,f). A number of OM pores extend along with the distribution of the OM, with evidence suggesting OM shrinkage (Figure 4c,g). Some of the large-scale near-elliptical OM pores are connected by slit-like OM pores (Figure 4a,h).

In the higher-porosity sample V2, inorganic pores such as interP pores dominate, while OM pores are less developed. Within the FOV, the OM pores are mainly slit-shaped (Figure 5j). The inorganic pores are mainly interP pores within clay minerals (Figure 5a,l), and interparticle pores are present at the edge of quartz grains (Figure 5c,d). Only a few intraP pores have developed (Figure 5k). Slit-like pores and fractures are well-developed, mostly formed between clay minerals and quartz grains. Some interP pores also develop between clay minerals and siderite (Figure 5d,k). There are also a small number of slit-like pores at the junction of OM and inorganic

minerals. Their length is generally up to several micrometers in dimension but can reach tens of micrometers.

For the OM-hosted pores in the low-porosity sample V1, most of the pore diameters are in the range 5−10 μm. Their main pore morphology includes slit-like, nearly circular, and irregular elliptical shapes. Nearly circular or elliptical OM pores exist predominantly in isolation, and their connectivity is poor. However, some slit-like OM pores connect isolated near-circular OM pores (Figure 4a,h). This phenomenon improves the local pore connectivity. Sample V2 contains predominantly pores within the inorganic MM with pore diameters in the range 5−20 μm. The morphology of the inorganic pores mainly includes needlelike, slit-like, and spindle-like. The pore connectivity in the transitional shale is mainly provided by microfractures or long slit-like pores. Partially developed interP pores between mineral grains are often connected to form grain boundary fractures (Figure 5k,l), with high local pore connectivity.

3.3. Three-Dimensional Reconstruction of the Pore System.
The results show that the OM is unevenly dispersed in the mineral matrix in irregular scattered clumps or strips. OM pores are mainly in the shape of needles or slits. Some pores are developed on the edges of OM and inorganic minerals. The 3D digital image of sample V1 is dominated by organic pores, while the 3D digital rock of sample V2 is dominated by inorganic pores (Figure 6). We reconstruct each
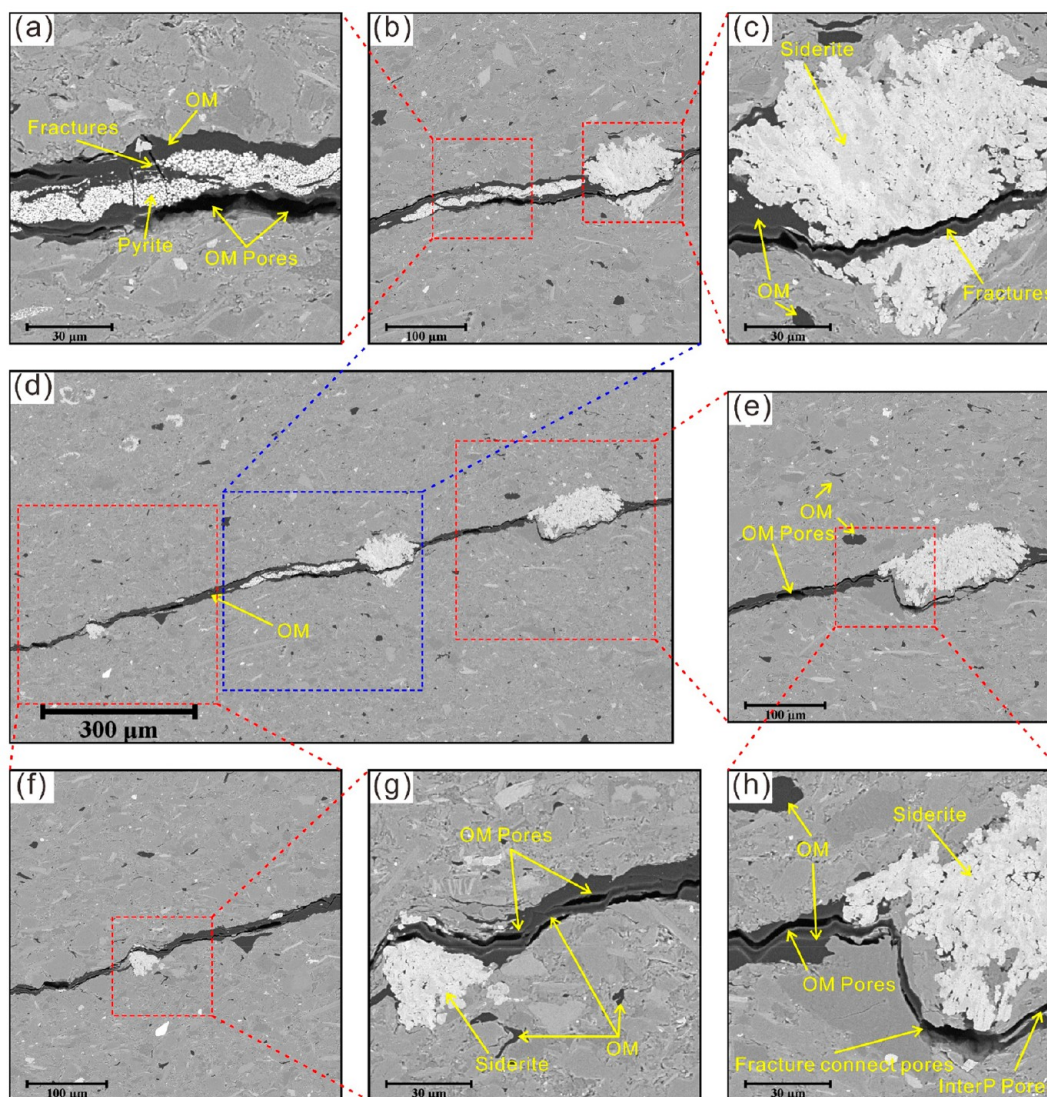
Figure 4. SEM images of low porosity and predominantly OM-hosted pores of sample V1 showing mineral compositions and different types of pores.

phase in the sample and generate the pore network model (PNM) using FIB-SEM data. In Figure 7, the processed digital rock (including 3D information for all phases) is visualized. Each phase (pores, OM, and mineral phase) and PNM are shown separately in Figure 8 and Figure 9.

Furthermore, we measured the volume fraction (vol %) of each phase by counting voxels, which are plotted in Figure 8 and Figure 9. In the digital image of sample V1, the pore volume accounts for 0.29%. The OM phase accounts for 3.11% by volume, and the mineral phase accounts for 96.62% (Figure 8). Pores are relatively concentrated within in the OM and at the contact between OM and clay minerals. The pore morphology is of mainly fracture-connected pores or needle-shaped OM pores. A few pores are bead- or grape-shaped and are scattered randomly in the OM. In the digital image of sample V2, the pores account for 4.22% of the volume (Figure 9). The mineral phase accounts for 95.78%. There is almost no OM in the 3D digital rock of sample V2, so it mainly contains inorganic pores. Some of the microfractures transect the entire sample volume of the digital rock.

3.4. Pore Size Distribution and Pore Morphology Based on FIB-SEM Data.
Here, analysis from high-resolution 3D nanotomographic images is reported for parameters including pore diameter and pore volume. The pore morphologic characteristics with the calculated shape factors are also discussed.

3.4.1. Pore Size Distribution. Pore size is classified using the classification scheme from the International Union of Pure and Applied Chemistry (IUPAC).[60] The IUPAC pore classification scheme classifies pores into four categories according to their diameter: micropores <2 nm, mesopores 2−50 nm, and macropores >50 nm in diameter, where pores less than 100 nm in diameter are classified as nanoscale pores.

Figure 10 shows the relationships among the pore volume, surface area, and pore equivalent diameter of the two samples. Each triangle or circle in the figure carries a characterization of a pore. Figure 11 is the cumulative histogram of the pore diameter distribution of the two samples. The pore size distribution in most OM-samples V1 is mainly concentrated in the 20−100 nm range. The smallest pore diameter is 12.4 nm, and the largest pore diameter is 568.3 nm. The average pore
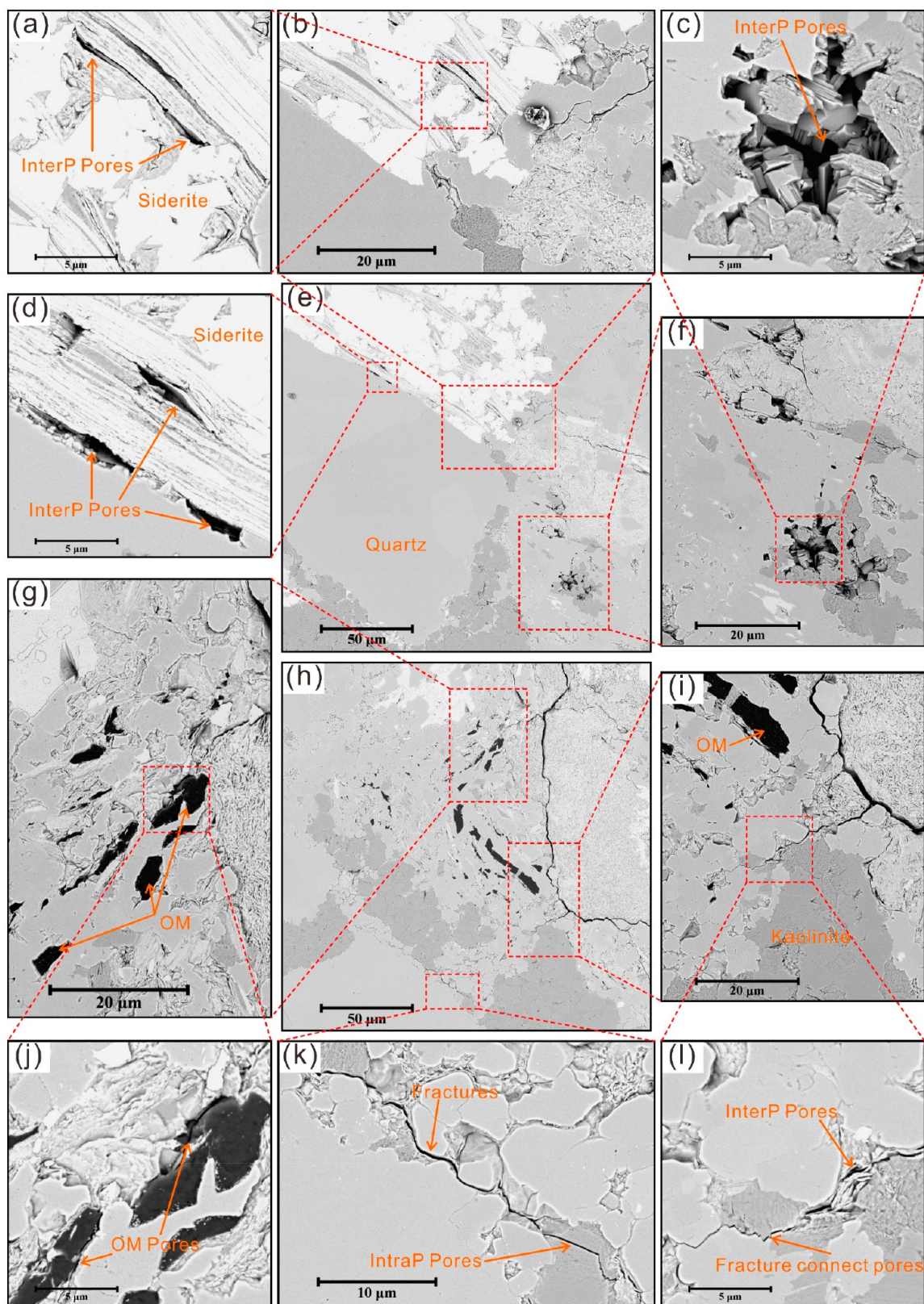
Figure 5. SEM images of high porosity and predominantly MM-hosted pores of sample V2 showing mineral compositions and different types of pores.

diameter is 97.7 nm (Figure 10a and Figure 11a). The average pore volume is 2.7×10^6 nm^3, and the average pore area is 1.14×10^5 nm^2. The number of mesopores (2−50 nm) account for 47.5% of the total number of pores, but their volume only

accounts for 0.4% of the total pore volume. The pore reservoir space is mainly provided by macropores (>50 nm).

The majority of pores in MM-sample V2 have an equivalent diameter of 30 to 200 nm. The minimum equivalent diameter
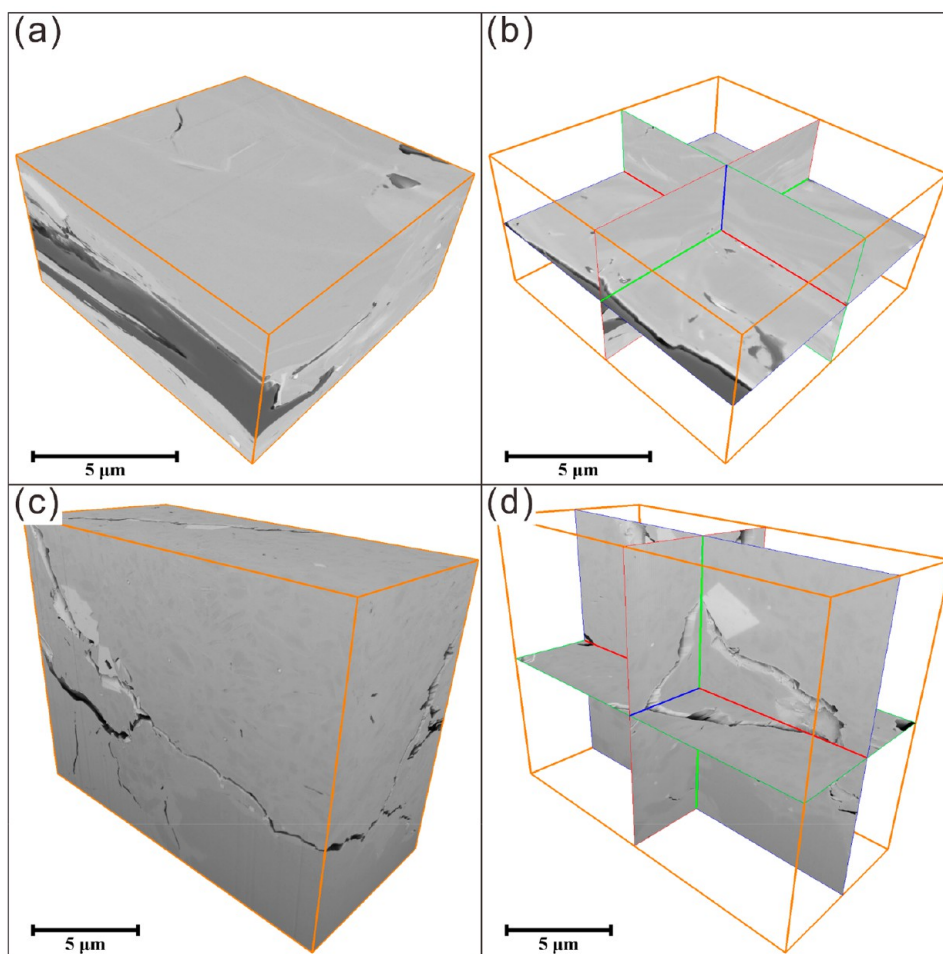
Figure 6. 3D spatial distribution of the samples from FIB-SEM (a) and (b) from the OM-hosted pores of sample V1; (c, d) MM-hosted pores of sample V2.
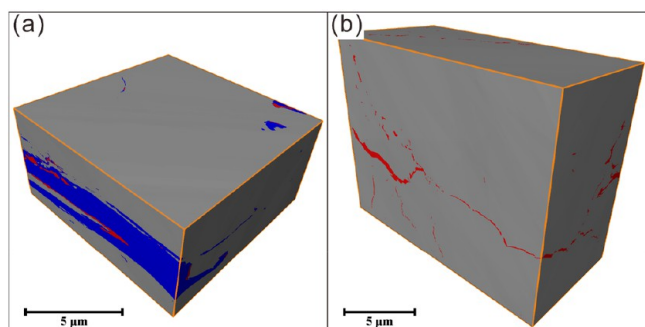

Figure 7. 3D model of the shale samples after image segmentation. (a) OM-sample V1; (b) MM-sample V2 (The red area represents pores, the blue area OM and the gray area the mineral phase.).

of pores is 34.8 nm, and the maximum equivalent diameter of pores is 1188.8 nm. The average pore diameter is 154.9 nm (Figure 10b and Figure 11b). The average pore volume is 19.6 × 10^6 nm^3, and the average pore area is 4.2 × 10^5 nm^2. The mesopore volume accounts for 0.07% of the total pore volume. And the number of mesopores accounts for only 39.5% of the total, which is less than that of OM-sample V1.

It can be concluded from Figure 10 and Figure 11 that the smaller the equivalent pore diameter or pore volume, the more concentrated the corresponding pore surface area distribution. The size of the inorganic pores in the MM-predominant digital

rock V2 is generally larger than that of the organic pores in the OM-predominant V1. Furthermore, sample V2 contains a higher proportion of pores with equivalent diameters >200 nm.

3.4.2. Pore Morphology. Most of the OM pores are spherical, nearly spherical, or slit-like. Some pores also develop at the junction of OM and inorganic minerals. Some of the OM pores are bead-shaped and are present in clusters. The main forms of inorganic pores (interP pores and intraP pores) are blade shape and as cracks. Most of the inorganic pores, especially those within clay minerals, are flatter than the OM pores.

We use the 3D pore structure parameters obtained by FIB-SEM data to calculate the shape factors of each pore and examine them as a distributed histogram. The pore distributions for different morphologies can be described by plotting the shape factor distribution histogram. As shown in Figure 12, the shape factor distributions of samples V1 and V2 are relatively similar. Most of the shape factors are between 1 and 2, indicating that most of the pores have a regular boundary, such as an ellipsoid, or are nearly spherical. In Figure 12, there are some large values (>40) for the shape factor of sample V1, indicating the presence of some extremely complex pore shapes in sample V1.
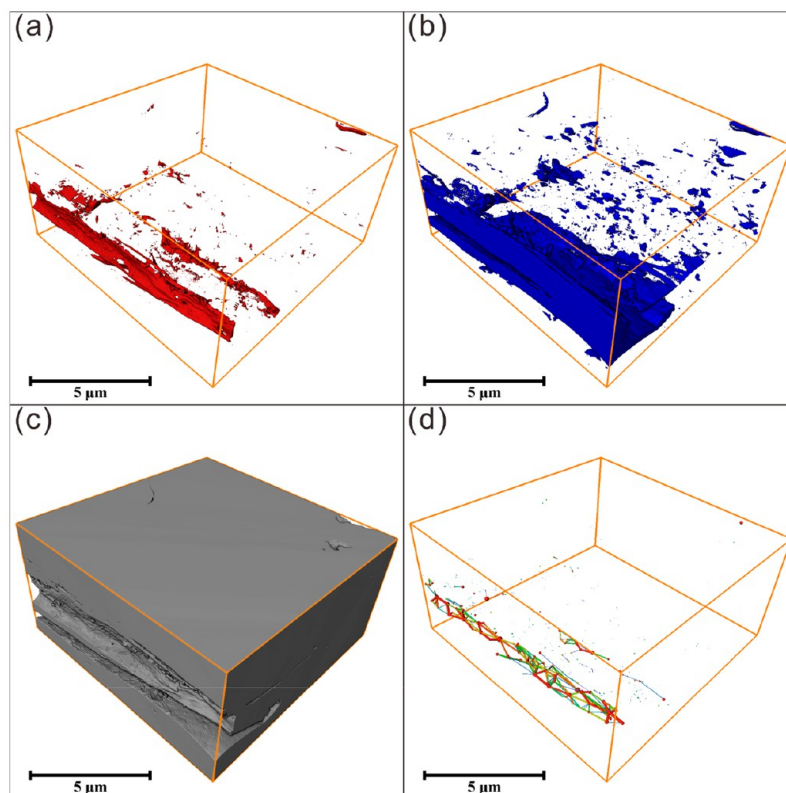
Figure 8. 3D visualization of pores, OM, and mineral phases (MM) of sample V1 based on FIB-SEM 3D nanotomography and the resulting pore network model.
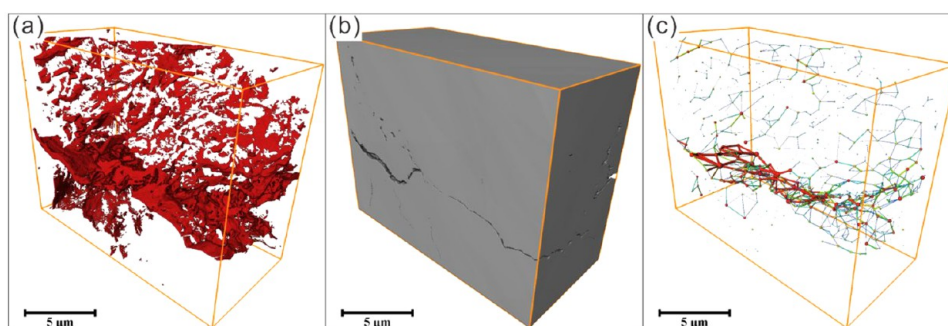

Figure 9. 3D visualization of pores, OM, and mineral phases of sample V2 based on FIB-SEM 3D nanotomography and the resulting pore network model.
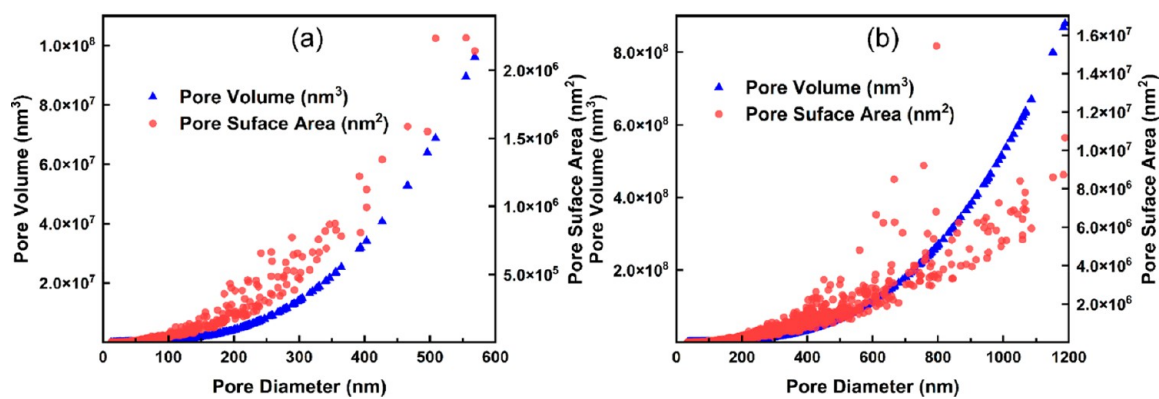

Figure 10. Relationship between pore volume, pore diameter, and pore surface areas. (a) OM-sample V1; (b) MM-sample V2.
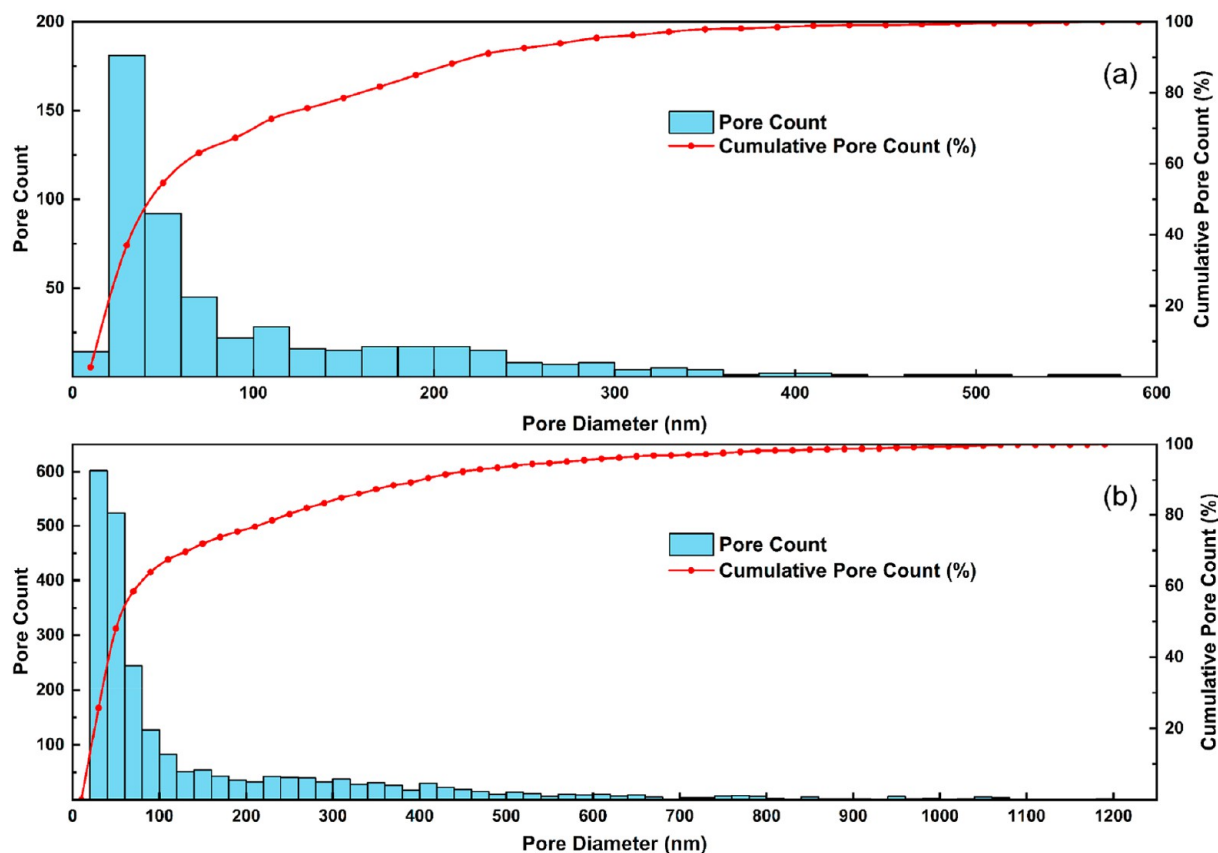
Figure 11. Pore size distributions (PSD) of the two samples. (a) OM-sample V1; (b) MM-sample V2.
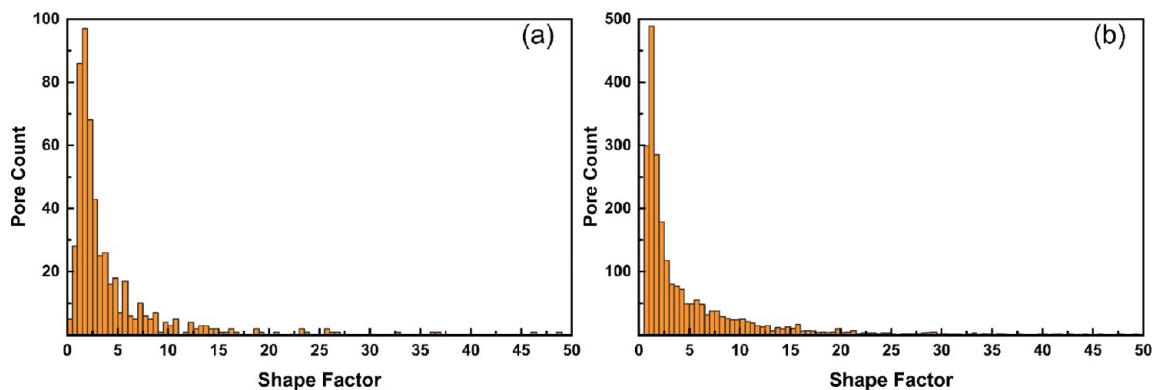

Figure 12. Histogram of pore shape factor distribution of sample by FIB-SEM data: (a) OM-sample V1; (b) MM-sample V2.

4. DISCUSSION

The pore and throat connections are discussed here by using the PNM data generated from the FIB-SEM observations. The coordination number of the pores is also used to evaluate the pore connectivity. Then, cubic sub-blocks extracted from the entire digital 3D rock are discussed with reference to the parameters of pore diameter, surface area, and volume, and an appropriate REV containing information on pore structures is proposed.

4.1. Pore Connectivity in 3D. The FIB-SEM data show that most of the pores in sample V1 exist in isolation and are not connected through any throats, although some pores are connected by a single throat. The connected pores account for 46% of the total number of pores, and their volume accounts

for 92.51% of the total. However, the distribution of connected pores is spatially concentrated, indicating that the overall connectivity of the pores is poor. The pore and throat diameters developed on the boundary between OM and inorganic mineral matters (MM) are relatively large. The pore connectivity is primarily provided by a fracture through the interior of the OM (Figure 8), with a few pores connected to the sample edge. There are several fractures in MM-predominant sample V2 connecting the internal pores and the sample edge. The connected pores account for 25.34% of the total number of pores, and the volume accounts for 98%. Although the proportion of connected pores in sample V2 is small, the proportion of volume is high, and the distribution of connected pores is extensive. Therefore, the overall connected
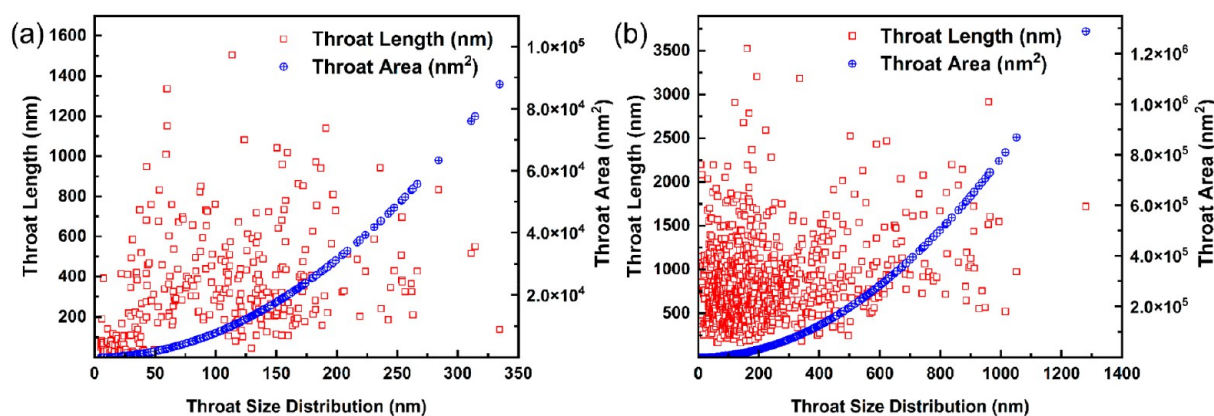
Figure 13. Relationship between the throat diameter, length, and surface area evaluated by the pore network model (PNM). (a) OM-sample V1; (b) MM-sample V2.

pore volume of sample V2 is much larger than that in sample V1.

As shown in Figure 13, the throat diameters (*x*-axis) and throat lengths (*y*-axis) within sample V2 are much larger than those within sample V1. The throat diameters of sample V1 are mainly concentrated in the range 10−200 nm, and the throat lengths are mainly concentrated below 600 nm (Figure 13a). The throat diameters of sample V2 are mainly concentrated in the range 10−400 nm, and the throat lengths are distributed between 250 and 1500 nm (Figure 13b). Therefore, from the perspective of the throat size, the pore connectivity in sample V2 is greater than that in sample V1. The proportion of isolated pores, those with a coordination number of 0, is 54% for V1 and 74.66% for V2. Figure 14 shows the distribution of

Figure 14. Pore network coordination numbers and proportions for the two samples.

the number for the two samples (except the situation with a coordination number of 0). Figure 14 shows the distribution of the coordination numbers for the two samples. The coordination number for the pores in sample V1 is mainly contained within the range 1−6, and the number of connected pores with a coordination number of 1 is a maximum (i.e., the mode). The coordination number of pores in sample V2 is mainly concentrated in the range 1−7, and the number of connected pores with a coordination number of 3 is a maximum (i.e., the mode). Most of the throat diameters and

lengths in the MM sample V2 are much higher than the throats in the OM sample V1, and the connected pore volume in the MM sample V2 is relatively higher.

The relative abundance of pore-connected domains is one of the important ways to determine the connectivity of pores in 3D space, as it can show the connectivity of pores both deterministically and intuitively. Pore-connected domains can be divided into dead (-end) unconnected domains (isolated pores) and live connected domains (connected pores).[61] The live connected domain is further divided into grade-1, grade-2, and grade-3 connected domains, according to different connectivity conditions. The grade-1 connected domain is composed of only two adjacent pores, and the connectivity range is small. The grade-2 connected domain is interconnected by more than two pores, but there is no second throat connection between the two pores. Its connectivity range is medium. The grade-3 connected domain is composed of a large number of pores connected by throats of various sizes and presents a network distribution in three-dimensional space. It has the widest range of connectivity.

After the Pore Network Model (PNM) is properly assembled as a ball-and-stick model carrying information on pores and throats, the connected pores are composed of grade-1, grade-2, and grade-3 connected domains. In sample V1, the connected domains of each grade are developed on the edge of the digital rock and have a concentrated distribution (Figure 15a). The pore connected domains of sample V2 comprise multiple network structures, and the connected domains at all grades are spread throughout the entire digital rock sample (Figure 15b). The connectivity of sample V2 is relatively higher.

4.2. REV Discussion. REV has been assessed in many studies for porous media such as shale but mostly using overall parameters such as porosity.[22−25] Using an overall parameter such as porosity to assess REV can be influenced by the nonhomogeneity of the porous material, which can affect the accuracy of the results. The REV assessment method used in this study focuses more on the characteristics of each pore itself. It is more accurate to assess the REV using the properties of each region as an evaluation parameter. This method helps to quickly understand the pore structure in rocks, and the REV assessed by this method is more consistent with the pore structure characteristics of this sample. The MM predominant sampled V2 was selected to determine the REV. In this study, the range of REV is bounded using the extreme value
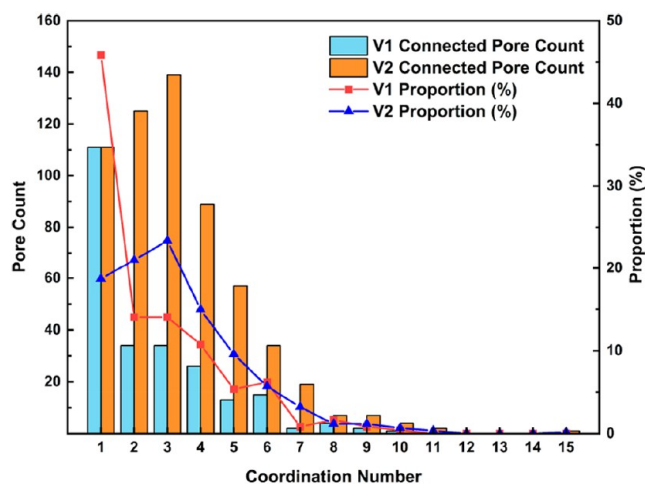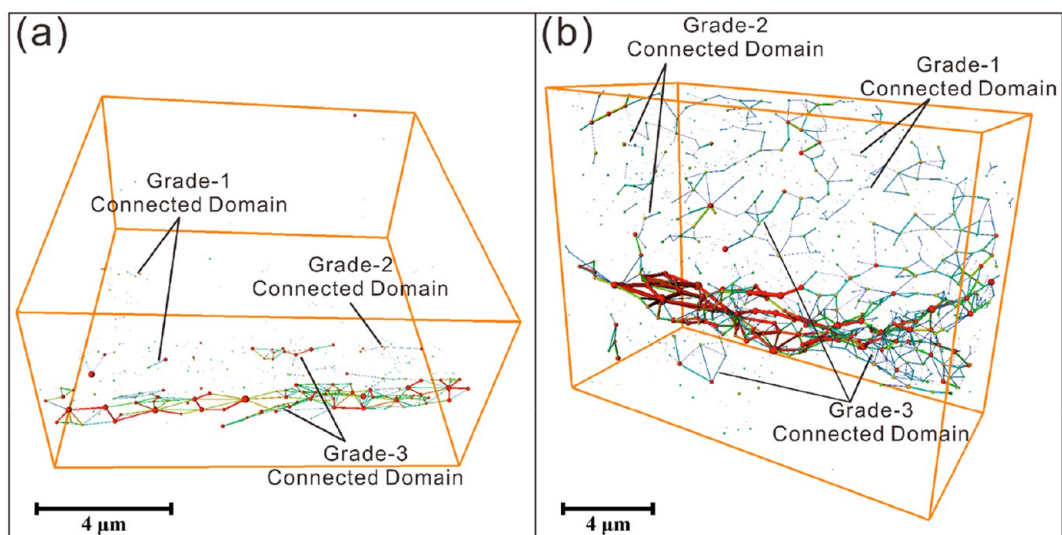
Figure 15. Connected domains in samples (a) OM-V1 and (b) MM-V2.
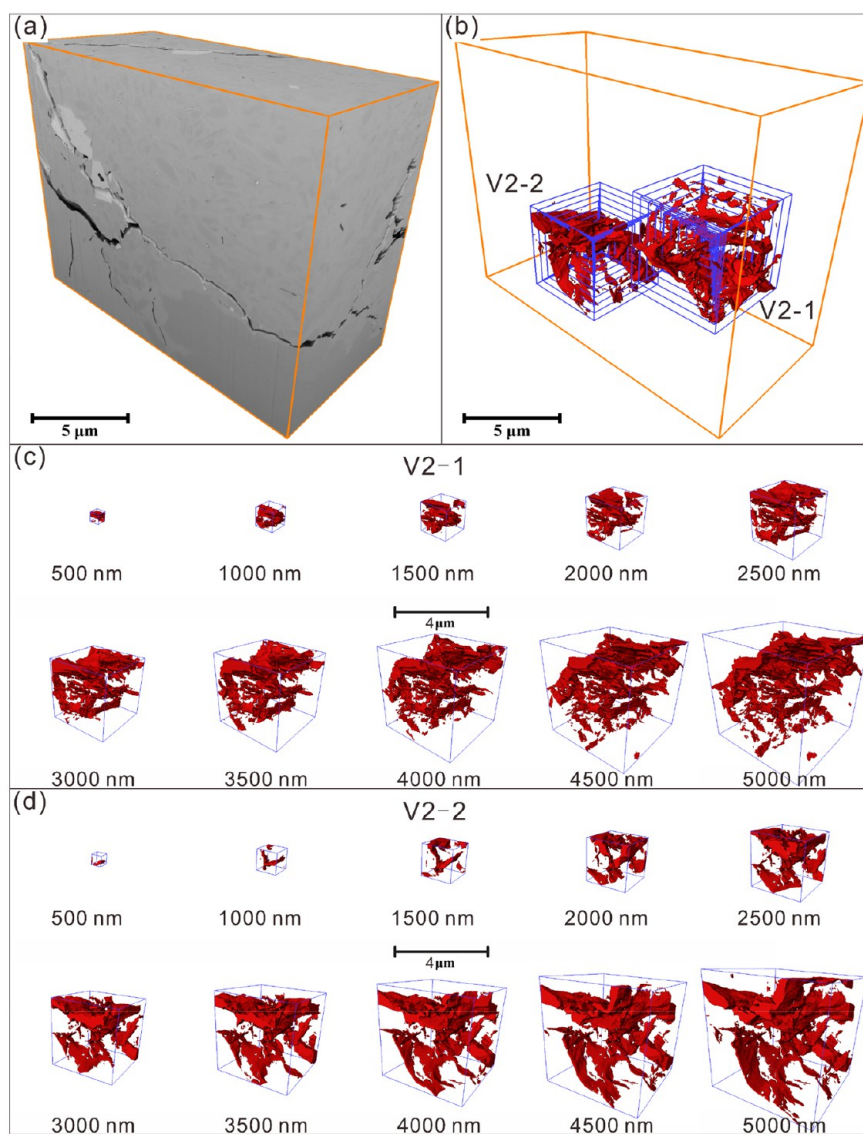

Figure 16. Location of the two selected regions in sample V2 and 3D visualization of pores within each cubic region.
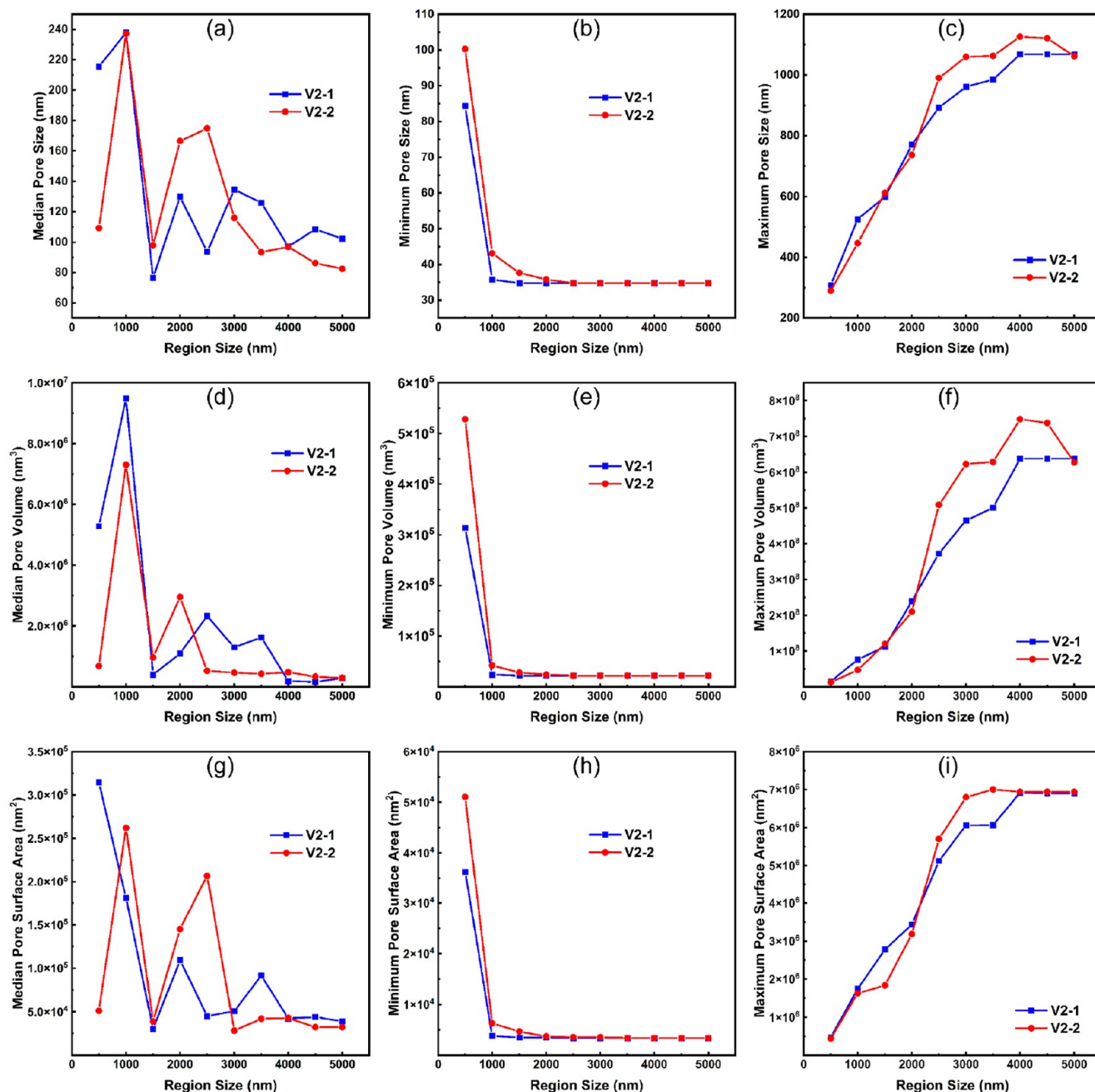
Figure 17. Correlation between region size and pore structure parameters. (a) Median pore size; (b) Minimum pore size; (c) Maximum pore size; (d) Median pore volume; (e) Minimum pore volume; (f) Maximum pore volume; (g) Median pore surface area; (h) Minimum pore surface area; (i) Maximum pore surface area.

parameters and the overall parameters in each region. As shown in Figure 16, in order to study the REV of the pore system, two different regions (both regions are cubes with side lengths of 5 μm) were selected. In these two regions, we take 10 cubic regions at equal intervals from the center of each region. The minimum region side length is 50 nm (50 pixels), and the maximum region side length is 5000 nm (500 pixels). The pores in the 20 digital rocks are extracted, and their pore structure parameters were counted. If the pore structural parameter is relatively stable with increasing cube size, the minimum corresponding volume was recorded as the REV. This guarantees the minimum REV for that particular parameter or family of parameters. We assume that the REV

is also consistent for derivative parameters, such as permeability, that depend on pore-size, -shape, and -connectivity.

As shown in Figure 17, from top to bottom are the pore diameter, pore volume, and pore surface area—and from left to right are the median, minimum, and maximum values of the pore structure parameters. With an increase in the edge length of the digital rock, the minimum values of various pore structure parameters tend to stabilize for a cubic edge-dimension >1500 nm (150 pixels). Since the lower limit of the minimum value is determined by the resolution of the digital rock, based on the FIB-SEM and the smallest pore that can be observed in the sample, the numerical coincidence of the two
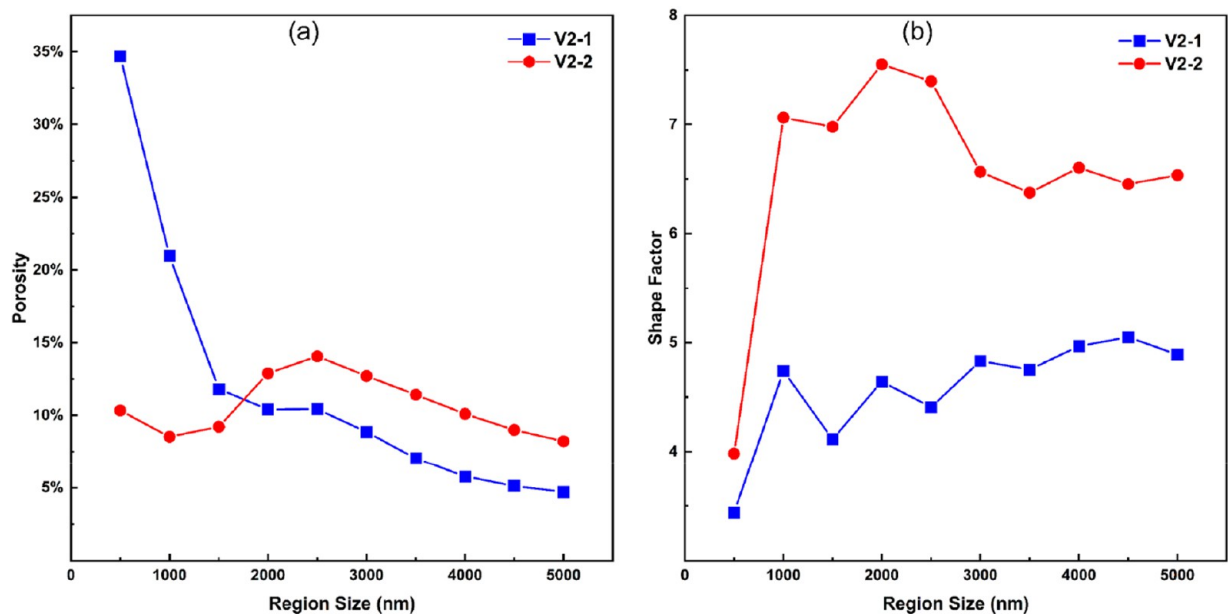
Figure 18. Correlation between region size and shale physical property. (a) Porosity; (b) Shape factor.

regions (red and blue lines in Figure 17) is good. The maximum value of the pore structure parameters is affected by the size and location of the study region, and the value fluctuates significantly when the region size is small. After 4000 nm (400 pixels), the maximum value of each pore structure parameter tends to be relatively stable (except for V2−2 in Figure 17f). The median number of pore structure parameters is not affected by the maximum parameter or minimal value, which can more accurately reflect the basic characteristics of the pore structure. Variations in its value also tend to stabilize around 4000 nm (400 pixels).

Figure 18 shows the relationship between the REV size, the porosity, and the average shape factor of the pores. The variation in porosity with the edge dimension of the REV is in poor agreement with other pore structure parameters. However, the relative variability also decreases around 4000 nm (400 pixels). The average shape factor for the pores can reflect the basic shape of the pores within the REV, to a certain extent. With an increment in the REV edge dimension, the relationship between the average shape factor and the other pore structure parameters tends to stabilize. Due to the strong heterogeneity of the pore structures in these samples, the calculation of REV based on parameters carrying no information on heterogeneity, e.g., porosity, volume of mineral matrix, or organic matter, are in jeopardy of missing information that reflects heterogeneity, such as the variation in pore shapes and structures.[53,62,63]

Through the statistics and analysis of various pore structure parameters, it is found that there is a uniform REV size for each pore structural parameter. It can be seen that the pore structure parameters basically converge and stabilize at 4000 nm (400 pixels). In the digital representation of MM-sample V2, 4000 nm (400 pixels) is the REV size based on basic pore structure parameters within this resolution and scale range.

5. CONCLUSIONS

While acquiring large-scale and high-resolution images using only a single imaging tool is feasible, there is typically a trade-off between the fine-scale resolution of the technique and the expanse of the field-of-view. Thus, we present a methodology to acquire and then define the appropriate minimum REV, different from commonly used large physical properties, such as porosities. This new method specifically considers pore structural parameters and focuses more on the characteristics of each pore.

Analysis by MAPS can recover high-resolution pore structure distributions over a broad range of scales from nm to μm. This approach can help provide a better understanding of heterogeneity in shales with regard to mineral composition as well as pore and fracture distributions. Two transitional shale samples show that the pores are mainly developed in the OM and as interparticle inorganic pores.

By constructing digital rock images from FIB-SEM, we can acquire the size, morphology, and connectivity of pores both in the OM and in the inorganic mineral matter. The porosities of the two digital rocks are 0.29% and 4.22%, respectively, with pore diameters ranging between 20 and 300 nm. Extracting cubic sub-blocks, ranging from 500 to 5000 nm in edge dimension, defines the minimum REV as ∼4000 nm, as measured using minimum and maximum pore sizes, surface areas, and shape factors.

Combined FIB and MAPS provide crucial insight into pore morphology and connectivity at multiple scales with the reconstructed digital rock used to determine representative REV sizes. Such results are useful in understanding the pore structure in tight rocks and for the rapid acquisition of pore structure distributions.

■ AUTHOR INFORMATION

Corresponding Author

Yong Li − *State Key Laboratory of Coal Resources and Safe Mining, College of Geosciences and Surveying Engineering, China University of Mining and Technology, Beijing 100083, China;* ◉ orcid.org/0000-0001-8859-156X;
Email: liyong@cumtb.edu.cn, cugbliyong@gmail.com

Authors

Jinfeng Xie − *State Key Laboratory of Coal Resources and Safe Mining, College of Geosciences and Surveying Engineering, China University of Mining and Technology, Beijing 100083, China;* ⊙ orcid.org/0000-0002-4543-123X

Derek Elsworth − *Department of Energy and Mineral Engineering, Geosciences, EMS Energy Institute and the G3 Center, Pennsylvania State University, University Park 16802 Pennsylvania, United States*

Zhejun Pan − *Key Laboratory of Continental Shale Hydrocarbon Accumulation and Efficient Development, Ministry of Education, Northeast Petroleum University, Daqing 163318 Heilongjiang, China*

Complete contact information is available at:
https://pubs.acs.org/10.1021/acs.energyfuels.3c03939

Notes

The authors declare no competing financial interest.

■ REFERENCES

(1) Anovitz, L. M.; Cole, D. R. Characterization and Analysis of Porosity and Pore Structures. *Rev. Mineral. Geochem.* **2015**, *80* (1), 61−164.

(2) Ross, D. J. K.; Bustin, R. M. Characterizing the Shale Gas Resource Potential of Devonian-Mississippian Strata in the Western Canada Sedimentary Basin: Application of an Integrated Formation Evaluation. *AAPG Bull.* **2008**, *92* (1), 87−125.

(3) Slatt, R. M.; O'Brien, N. R. Pore Types in the Barnett and Woodford Gas Shales: Contribution to Understanding Gas Storage and Migration Pathways in Fine-Grained Rocks. *AAPG Bull.* **2011**, *95* (12), 2017−2030.

(4) Lai, J.; Wang, G.; Wang, Z.; Chen, J.; Pang, X.; Wang, S.; Zhou, Z.; He, Z.; Qin, Z.; Fan, X. A Review on Pore Structure Characterization in Tight Sandstones. *Earth-Sci. Rev.* **2018**, *177*, 436−457.

(5) Liu, B.; Mastalerz, M.; Schieber, J. SEM Petrography of Dispersed Organic Matter in Black Shales: A Review. *Earth-Sci. Rev.* **2022**, *224*, 103874.

(6) Wu, J.; Yuan, Y.; Niu, S.; Wei, X.; Yang, J. Multiscale Characterization of Pore Structure and Connectivity of Wufeng-Longmaxi Shale in Sichuan Basin, China. *Mar. Pet. Geol.* **2020**, *120*, 104514.

(7) Yang, C.; Zhang, J.; Wang, X.; Tang, X.; Chen, Y.; Jiang, L.; Gong, X. Nanoscale Pore Structure and Fractal Characteristics of a Marine-Continental Transitional Shale: A Case Study from the Lower Permian Shanxi Shale in the Southeastern Ordos Basin, China. *Mar. Pet. Geol.* **2017**, *88*, 54−68.

(8) Iglauer, S.; Akhondzadeh, H.; Abid, H.; Paluszny, A.; Keshavarz, A.; Ali, M.; Giwelli, A.; Esteban, L.; Sarout, J.; Lebedev, M. Hydrogen Flooding of a Coal Core: Effect on Coal Swelling. *Geophys. Res. Lett.* **2022**, *49* (6), No. e2021GL096873.

(9) Arif, M.; Mahmoud, M.; Zhang, Y.; Iglauer, S. X-Ray Tomography Imaging of Shale Microstructures: A Review in the Context of Multiscale Correlative Imaging. *Int. J. Coal Geol.* **2021**, *233*, 103641.

(10) Zhang, J.; Tang, Y.; He, D.; Sun, P.; Zou, X. Full-Scale Nanopore System and Fractal Characteristics of Clay-Rich Lacustrine Shale Combining FE-SEM, Nano-CT, Gas Adsorption and Mercury Intrusion Porosimetry. *Appl. Clay Sci.* **2020**, *196*, 105758.

(11) Khaledi, K.; Hamdi, P.; Winhausen, L.; Jalali, M.; Jaeggi, D.; Amann, F. Unloading Induced Absolute Negative Pore Pressures in a Low Permeable Clay Shale. *Eng. Geol.* **2021**, *295*, 106451.

(12) Liu, K.; Sheng, J. J.; Zhang, Z. A Simulation Study of the Effect of Clay Swelling on Fracture Generation and Porosity Change in Shales under Stress Anisotropy. *Eng. Geol.* **2020**, *278*, 105829.

(13) Wu, Y.; Tahmasebi, P.; Yu, H.; Lin, C.; Wu, H.; Dong, C. Pore-Scale 3D Dynamic Modeling and Characterization of Shale Samples: Considering the Effects of Thermal Maturation. *J. Geophys. Res. Solid Earth* **2020**, *125* (1), No. e2019JB018309.

(14) Medina, F. J.; Jausoro, I.; Floridia Addato, M. A.; Rodriguez, M. J.; Tomassini, F. G.; Caneiro, A. On the Evaluation of Representative Elementary Area for Porosity in Shale Rocks by Field Emission Scanning Electron Microscopy. *Energy* **2022**, *253*, 124141.

(15) Bai, B.; Elgmati, M.; Zhang, H.; Wei, M. Rock Characterization of Fayetteville Shale Gas Plays. *Fuel* **2013**, *105*, 645−652.

(16) Thibodeaux, T. W.; Sheng, Q.; Thompson, K. E. Rapid Estimation of Essential Porous Media Properties Using Image-Based Pore-Scale Network Modeling. *Ind. Eng. Chem. Res.* **2015**, *54* (16), 4474−4486.

(17) Nordahl, K.; Ringrose, P. S. Identifying the Representative Elementary Volume for Permeability in Heterolithic Deposits Using Numerical Rock Models. *Math. Geosci.* **2008**, *40* (7), 753−771.

(18) Singh, A.; Regenauer-Lieb, K.; Walsh, S. D. C.; Armstrong, R. T.; van Griethuysen, J. J. M.; Mostaghimi, P. On Representative Elementary Volumes of Grayscale Micro-CT Images of Porous Media. *Geophys. Res. Lett.* **2020**, *47* (15), No. e2020GL088594.

(19) Jackson, S. J.; Lin, Q.; Krevor, S. Representative Elementary Volumes, Hysteresis, and Heterogeneity in Multiphase Flow From the Pore to Continuum Scale. *Water Resour. Res.* **2020**, *56* (6), No. e2019WR026396.

(20) Chen, Y.; Jiang, C.; Leung, J. Y.; Wojtanowicz, A. K.; Zhang, D. Multiscale Characterization of Shale Pore-Fracture System: Geological Controls on Gas Transport and Pore Size Classification in Shale Reservoirs. *J. Pet. Sci. Eng.* **2021**, *202*, 108442.

(21) Wu, M.; Wu, J.; Wu, J.; Hu, B. X. A New Criterion for Determining the Representative Elementary Volume of Translucent Porous Media and Inner Contaminant. *Hydrol. Earth Syst. Sci.* **2020**, *24* (12), 5903−5917.

(22) Al-Raoush, R.; Papadopoulos, A. Representative Elementary Volume Analysis of Porous Media Using X-Ray Computed Tomography. *Powder Technol.* **2010**, *200* (1), 69−77.

(23) Mostaghimi, P.; Blunt, M. J.; Bijeljic, B. Computations of Absolute Permeability on Micro-CT Images. *Math. Geosci.* **2013**, *45* (1), 103−125.

(24) Ma, L.; Taylor, K. G.; Lee, P. D.; Dobson, K. J.; Dowey, P. J.; Courtois, L. Novel 3D Centimetre-to Nano-Scale Quantification of an Organic-Rich Mudstone: The Carboniferous Bowland Shale, Northern England. *Mar. Pet. Geol.* **2016**, *72*, 193−205.

(25) Wang, Y.; Wang, L.; Wang, J.; Jiang, Z.; Wang, C.-C.; Fu, Y.; Song, Y.-F.; Wang, Y.; Liu, D.; Jin, C. Multiscale Characterization of Three-Dimensional Pore Structures in a Shale Gas Reservoir: A Case Study of the Longmaxi Shale in Sichuan Basin, China. *J. Nat. Gas Sci. Eng.* **2019**, *66*, 207−216.

(26) Loucks, R. G.; Ruppel, S. C. Mississippian Barnett Shale: Lithofacies and Depositional Setting of a Deep-Water Shale-Gas Succession in the Fort Worth Basin, Texas. *AAPG Bull.* **2007**, *91* (4), 579−601.

(27) Yang, R.; Hu, Q.; He, S.; Hao, F.; Guo, X.; Yi, J.; Sun, M. Wettability and Connectivity of Overmature Shales in the Fuling Gas Field, Sichuan Basin (China). *AAPG Bull.* **2019**, *103* (3), 653−689.

(28) Guan, Q.; Lü, X.; Dong, D.; Cai, X. Origin and Significance of Organic-Matter Pores in Upper Ordovician Wufeng-Lower Silurian Longmaxi Mudstones, Sichuan Basin. *J. Pet. Sci. Eng.* **2019**, *176*, 554−561.

(29) Zhang, Q.; Fan, X.; Chen, P.; Ma, T.; Zeng, F. Geomechanical Behaviors of Shale after Water Absorption Considering the Combined Effect of Anisotropy and Hydration. *Eng. Geol.* **2020**, *269*, 105547.

(30) Meng, Q.; Hao, F.; Tian, J. Origins of Non-Tectonic Fractures in Shale. *Earth-Sci. Rev.* **2021**, *222*, 103825.

(31) Jiang, X.; Deng, S.; Li, H.; Zuo, H. Characterization of 3D Pore Nanostructure and Stress-Dependent Permeability of Organic-Rich Shales in Northern Guizhou Depression, China. *J. Rock Mech. Geotech. Eng.* **2022**, *14* (2), 407−422.

(32) Li, G.; Qin, Y.; Wu, M.; Zhang, B.; Wu, X.; Tong, G.; Liu, J. The Pore Structure of the Transitional Shale in the Taiyuan Formation, Linxing Area, Ordos Basin. *J. Pet. Sci. Eng.* **2019**, *181*, 106183.

(33) Li, Y.; Xu, L.; Chen, J.; Zhang, W.; Elsworth, D. Hydration of Transitional Shale and Evolution of Physical Properties Constrained by Concurrent NMR and Acoustic Observations. *Energy Fuels* **2023**, *37* (11), 7809−7822.

(34) Dou, W.; Liu, L.; Wu, K.; Xu, Z.; Feng, X. Diagenesis of Tight Oil Sand Reservoirs: Upper Triassic Tight Sandstones of Yanchang Formation in Ordos Basin, China. *Geol. J.* **2018**, *53* (2), 707−724.

(35) Li, Y.; Wang, Z.; Wu, P.; Meng, S. Paleoenvironment Reconstruction of the Upper Paleozoic in the Linxing Area, Northeastern Ordos Basin, China. *AAPG Bull.* **2021**, *105* (12), 2545−2574.

(36) Liu, C.; Huang, L.; Zhang, D.; Zhao, J.; Deng, Y.; Guo, P.; Huang, Y.; Wang, J. Genetic Causes of Oil-Rich and Oil-Poor Reservoirs: Implications from Two Cenozoic Basins in the Eastern North China Craton. *Sci. China Earth Sci.* **2018**, *61* (12), 1910−1931.

(37) Ahmad, M.; Haghighi, M. Mineralogy and Petrophysical Evaluation of Roseneath and Murteree Shale Formations, Cooper Basin, Australia Using QEMSCAN and CT-Scanning. In *All Days*; SPE: Perth, Australia, 2012; p SPE-158461-MS. DOI: 10.2118/158461-MS.

(38) Alotoom, A.; Shawabkeh, R.; Alharahsheh, A.; Shawaqfeh, A. The Chemistry of Minerals Obtained from the Combustion of Jordanian Oil Shale. *Energy* **2005**, *30* (5), 611−619.

(39) Grauch, R.; Eberl, D.; Butcher, A.; Botha, P. Quantitative Mineralogy of Fine-Grained Sedimentary Rocks: A Preliminary Look at QEMSCAN®. *Microsc. Microanal.* **2008**, *14* (S2), 532−533.

(40) Wu, T.; Zhao, J.; Zhang, W.; Zhang, D. Nanopore Structure and Nanomechanical Properties of Organic-Rich Terrestrial Shale: An Insight into Technical Issues for Hydrocarbon Production. *Nano Energy* **2020**, *69*, 104426.

(41) Saif, T.; Lin, Q.; Butcher, A. R.; Bijeljic, B.; Blunt, M. J. Multi-Scale Multi-Dimensional Microstructure Imaging of Oil Shale Pyrolysis Using X-Ray Micro-Tomography, Automated Ultra-High Resolution SEM, MAPS Mineralogy and FIB-SEM. *Appl. Energy* **2017**, *202*, 628−647.

(42) Shao, X.; Pang, X.; Li, Q.; Wang, P.; Chen, D.; Shen, W.; Zhao, Z. Pore Structure and Fractal Characteristics of Organic-Rich Shales: A Case Study of the Lower Silurian Longmaxi Shales in the Sichuan Basin, SW China. *Mar. Pet. Geol.* **2017**, *80*, 192−202.

(43) Li, Y.; Yang, J.; Pan, Z.; Tong, W. Nanoscale Pore Structure and Mechanical Property Analysis of Coal: An Insight Combining AFM and SEM Images. *Fuel* **2020**, *260*, 116352.

(44) Lemmens, H.; Richards, D. Multiscale Imaging of Shale Samples in the Scanning Electron Microscope. *AAPG Mem.* **2013**, *102*, 27−35.

(45) Zhou, S.; Yan, G.; Xue, H.; Guo, W.; Li, X. 2D and 3D Nanopore Characterization of Gas Shale in Longmaxi Formation Based on FIB-SEM. *Mar. Pet. Geol.* **2016**, *73*, 174−180.

(46) Zhou, S.; Liu, D.; Cai, Y.; Yao, Y.; Li, Z. 3D Characterization and Quantitative Evaluation of Pore-Fracture Networks of Two Chinese Coals Using FIB-SEM Tomography. *Int. J. Coal Geol.* **2017**, *174*, 41−54.

(47) Goral, J.; Walton, I.; Andrew, M.; Deo, M. Pore System Characterization of Organic-Rich Shales Using Nanoscale-Resolution 3D Imaging. *Fuel* **2019**, *258*, 116049.

(48) Goral, J.; Miskovic, I.; Gelb, J.; Andrew, M. Correlative XRM and FIB-SEM for (Non)Organic Pore Network Modeling in Woodford Shale Rock Matrix. In *International Petroleum Technology Conference*; Doha, Qatar, December 6−9, 2015; IPTC, 2015. DOI: 10.2523/IPTC-18477-MS

(49) Wang, Y.; Pu, J.; Wang, L.; Wang, J.; Jiang, Z.; Song, Y.-F.; Wang, C.-C.; Wang, Y.; Jin, C. Characterization of Typical 3D Pore Networks of Jiulaodong Formation Shale Using Nano-Transmission X-Ray Microscopy. *Fuel* **2016**, *170*, 84−91.

(50) Blott, S. J.; Pye, K. Particle Shape: A Review and New Methods of Characterization and Classification. *Sedimentology* **2008**, *55* (1), 31−63.

(51) Thermo Fisher. *User's Guide Avizo Software 2019*; Konrad-Zuse-Zentrum für Informationstechnik Berlin (ZIB): Germany, 2019.

(52) Bear, J. *Dynamic of Fluids in Porous Media*; American Elsevier Publishing Company: New York, 1972.

(53) Adeleye, J. O.; Akanji, L. T. Pore-Scale Analyses of Heterogeneity and Representative Elementary Volume for Unconventional Shale Rocks Using Statistical Tools. *J. Pet. Explor. Prod. Technol.* **2018**, *8* (3), 753−765.

(54) Saraji, S.; Piri, M. High-Resolution Three-Dimensional Characterization of Pore Networks in Shale Reservoir Rocks. In *Proceedings of the 2nd Unconventional Resources Technology Conference*; American Association of Petroleum Geologists: Denver, CO, 2014. DOI: 10.15530/urtec-2014-1870621.

(55) Ji, L.; Lin, M.; Cao, G.; Jiang, W. A Multiscale Reconstructing Method for Shale Based on SEM Image and Experiment Data. *J. Pet. Sci. Eng.* **2019**, *179*, 586−599.

(56) Liu, T.; Jin, X.; Wang, M. Critical Resolution and Sample Size of Digital Rock Analysis for Unconventional Reservoirs. *Energies* **2018**, *11* (7), 1798.

(57) Wu, H.; Yao, Y.; Zhou, Y.; Qiu, F. Analyses of Representative Elementary Volume for Coal Using X-Ray *μ*-CT and FIB-SEM and Its Application in Permeability Predication Model. *Fuel* **2019**, *254*, 115563.

(58) Loucks, R. G.; Reed, R. M.; Ruppel, S. C.; Jarvie, D. M. Morphology, Genesis, and Distribution of Nanometer-Scale Pores in Siliceous Mudstones of the Mississippian Barnett Shale. *J. Sediment. Res.* **2009**, *79*, 848−861.

(59) Loucks, R.; Reed, R.; Ruppel, S.; Hammes, U. Spectrum of Pore Types and Networks in Mudrocks and a Descriptive Classification for Matrix Related Pores. *AAPG Bull.* **2012**, *96*, 1071−1098.

(60) Rouquerol, J.; Avnir, D.; Fairbridge, C. W.; Everett, D. H.; Haynes, J. M.; Pernicone, N.; Ramsay, J. D. F.; Sing, K. S. W.; Unger, K. K. Recommendations for the Characterization of Porous Solids (Technical Report). *Pure Appl. Chem.* **1994**, *66*, 1739−1758.

(61) Sun, L.; Wang, X.; Jin, X.; Li, J.; Wu, S. Three Dimensional Characterization and Quantitative Connectivity Analysis of Micro/Nano Pore Space. *Pet. Explor. Dev.* **2016**, *43* (3), 537−546.

(62) Kelly, S.; El-Sobky, H.; Torres-Verdín, C.; Balhoff, M. T. Assessing the Utility of FIB-SEM Images for Shale Digital Rock Physics. *Adv. Water Resour.* **2016**, *95*, 302−316.

(63) Tang, X.; Jiang, Z.; Li, Z.; Gao, Z.; Bai, Y.; Zhao, S.; Feng, J. The Effect of the Variation in Material Composition on the Heterogeneous Pore Structure of High-Maturity Shale of the Silurian Longmaxi Formation in the Southeastern Sichuan Basin, China. *J. Nat. Gas Sci. Eng.* **2015**, *23*, 464−473.